Supporting Information

Experimental section

Materials

Bismuth nitrate ($Bi(NO_3)_3.5H_2O$), Cobalt nitrate ($Co(NO_3)_2.6H_2O$), Sodium Hydroxide (NaOH), Sodium Bromide (NaBr), Absolute ethanol (CH_3CH_2OH), Mannitol, cetyltrimethylammonium bromide (CTAB) and pH paper were obtained from Sinopharm Chemical, 2-Methylimidazole (2-MeIm) was purchased from Shanghai Aladdin Biochemical Technology, Polyvinylpyrrolidone (PVP) was gotten from Sigma-Aldrich. In this work, all of chemical reagents were analytically pure and employed without further purification.

Synthesis of Co-ZIF template material

First, 2-MeIm (9 g) was dispersed in 90 mL deionized water to form Solution A. Then $Co(NO_3)_2·6H_2O$ (0.5 g) was dispersed in 10 mL deionized water to form Solution B, both being stirred for 10 min. Solution B was poured into solution A and stirred for 2 min, then 10 mL cetyltrimethylammonium bromide (CTAB) was added into the mixed solution, and stirring was continued for 12 h. Afterwards, the mixture was centrifuged, washed with anhydrous ethanol for three times. Finally, the product was dried in an electrothermal constant temperature blast drying oven at 45 °C for 6 h to obtain Co-ZIF template material.

Synthesis of Co-ZIF-derived porous carbon (Co-PC) material

50 mg of dried Co-ZIF template material was weighed and placed in a tube furnace. Subsequently, the sample was calcined at 430 °C for 6 hours with a heating rate of 2 °C/min under a flowing N_2 atmosphere to obtain Co-PC material.

Synthesis of $Bi_{12}O_{17}Br_2$ (BOB) nanotubes

The $Bi_{12}O_{17}Br_2$ nanotubes were synthesized by one-pot solvothermal method, 0.2425 g $Bi(NO_3)_2·5H_2O$ and 0.2 g PVP were added to 15 mL (0.1 mol/L) mannitol solution, and ultrasonically dispersed to form solution A.

Similarly, 0.0514 g NaBr was added to 4 mL (0.1 mol/L) mannitol solution, and ultrasonically dispersed to form solution B. Then, solution B was dropped into solution A, the pH value of the above solution was tuned to 12.5 with NaOH solution (2 mol/L) and stirred it for another 30 min. Finally, the solution was poured into a 25 mL Teflon lined steel autoclave and reacted at 160 °C for 3 h. After cooling, the mixture was centrifuged, washed with anhydrous ethanol for several times. Finally, the product was dried in an electrothermal constant temperature blast drying oven at 45 °C for 6 h. The obtained material was named as BOB nanotubes for further experiments.

Synthesis of porous carbon material coupled $Bi_{12}O_{17}Br_2$ nanotubes (Co-PC/BOB) composites

Similarly, the solution B mentioned above was dropped into solution A, the pH value of the above solution was tuned to 12.5 with NaOH solution (2 mol/L) and stirred it for another 30 min. Then Co-PC material corresponding to the doping ratio (1 wt%) was added to the solution and stirred for 30 min. Finally, the solution was poured into a 25 mL Teflon lined steel autoclave and reacted at 160 °C for 3 h. After cooling, the mixture was centrifuged, washed with anhydrous ethanol for several times. Finally, the product was dried in a electrothermal constant temperature blast drying oven at 45 °C for 6 h. The obtained material was named as Co-PC/BOB-2 composite for further experiments. By tuning the introduced amount of Co-PC material to 0.5 wt.% or 3 wt.%, the obtained materials were named as Co-PC/BOB-1 or Co-PC/BOB-3 composite, respectively. The obtained materials were collected for further experiments.

Characterizations

The X-ray diffraction (XRD) patterns were reflected by Shimadzu XRD-6000 X-ray diffractometer with a Cu-Kα radiation source. The scanning electron microscopy (SEM) was taken on JSM-7800F and ThermoFisher Apreo S HiVac. The Transmission electron microscopy (TEM) images were characterized by JEOL-JEM-2100. The high-resolution TEM (HR-TEM)

micrographs were obtained by FEI Tecnai G2 F20 S-TWIN Electron Microscope. The UV-vis diffuse reflectance spectra (DRS) were recorded using a Shimadzu UV-2450 spectrometer. The Fourier transform infrared (FT-IR) spectra were conducted on Nexus 470 FT-IR spectrometer. The Raman spectra were obtained using ThermoFisher DXR Laser Raman Spectrometer. The X-ray photoelectron spectroscopy (XPS) was investigated by PHI5300 instrument with a Mg Kα source. The nitrogen adsorption and desorption isotherms were measured by TriStar II 3020 Surface Area and Porosity Analyzer. The carbon dioxide adsorption isotherms were obtained by instrument of Micromeritics Instrument Corporation. The in-situ FT-IR spectra were acquired with a ThermoFisher Nicolet iZ10. The Laser-induced fluorescence spectra were recorded using a Varian Cary Eclipse spectrometer. The Electrochemical studies were conducted by electrochemical workstation (CHI760E) with a three-electrode configuration. The conductive glass (1 cm × 3 cm) with dispersed catalysts as a working electrode. The Pt rod acted as a counter electrode, and Ag/AgCl electrode with saturated KCl solution was used as a reference electrode. The photocurrent responses curves were measured in 0.1 mol/L phosphate buffer solution (pH = 7), using a 300 W Xenon lamp as the light source during test. The electrochemical impedance spectra (EIS) were performed in a prepared electrochemical impedance solution (0.1 mol/L KCl solution, containing 5 mmol $Fe(CN)_6^{3-}$ /$Fe(CN)_6^{4-}$. The Mott-Schottky plots were obtained in 0.2 mol/L Na_2SO_4 solution with an amplitude of 5 mV, the test frequency was kept at 500, 1000, and 2000 Hz successively.

Photocatalytic CO_2 reduction measurement

The photocatalytic CO_2 reaction performance of the as-prepared materials was evaluated using a Labsolar-6A online gas system (Perfectlight, China). Generally, 20 mg catalyst was dispersed in a quartz reactor with 40 mL deionized water. The overall reaction system was evacuated to 0 kPa, and then the high purity CO_2 gas (99.99%) was injected until the system pressure reached 88 kPa. A 300 W Xenon lamp (PLS-SXE 300D (BF), Perfectlight,

China) was used as the light source. The photocatalytic reaction temperature was maintained at 5 °C by cooling the water circulation system which can promote the adsorption of CO_2. After the reaction, the gas products were quantified through Gas chromatography (FULI GC9790II, China). The CO, CH_4, C_2H_6 and C_2H_4 can be identified via a frame ionization detector (FID), and the H_2, O_2 and N_2 can be identified via a thermal conductivity detector (TCD). A complete product distribution diagram and the detection limitations of various products were shown in **Figure S1** and **Table S1**.

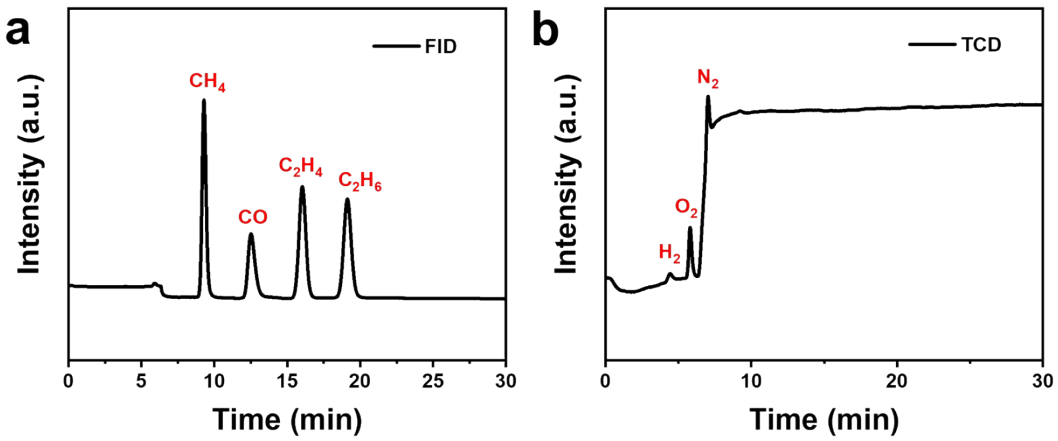

Figure S1. (a) Product Distribution Chart Detectable by FID Detector, (b) Product Distribution Chart Detectable by TCD Detector.

Table S1. The detection limitations of various products.

Product	CO	CH_4	C_2H_4	C_2H_6	H_2	O_2
Detection limits ($\mu mol\ g^{-1}$)	0.17857	0.3125	0.35714	0.33333	25	3.125

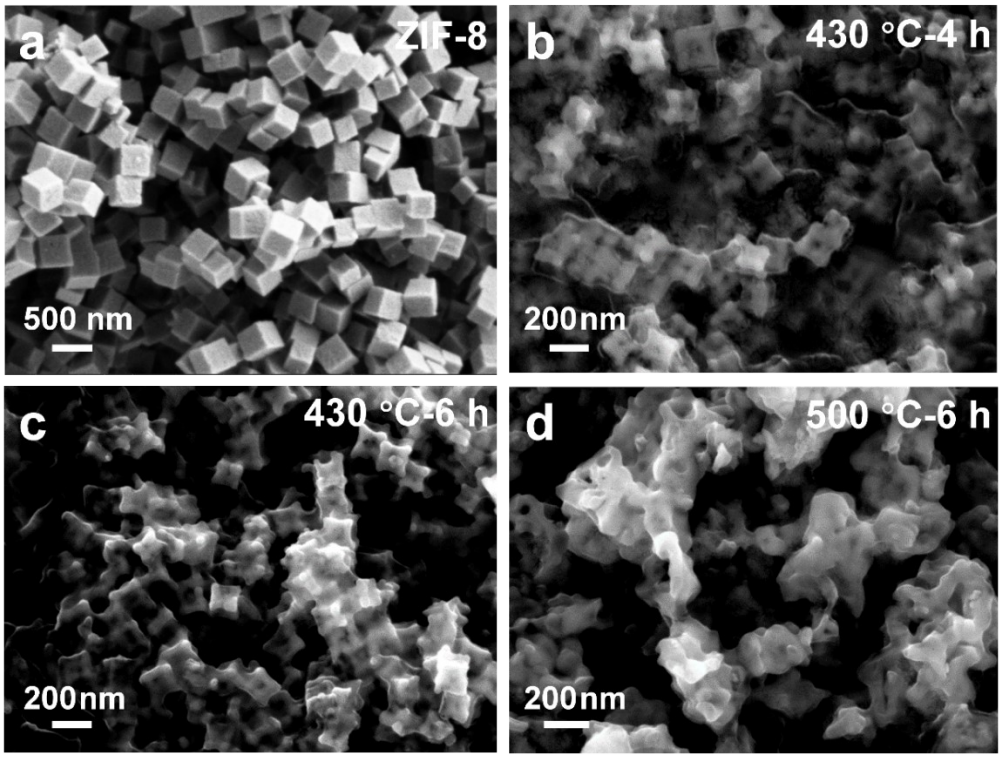

Figure S2. SEM images of (a) Co-ZIF precursor and the products of Co-ZIF precursor calcined at (b) 430 °C for 4 h，(c) 430 °C for 6 h, and (d) 500 °C for 6 h.

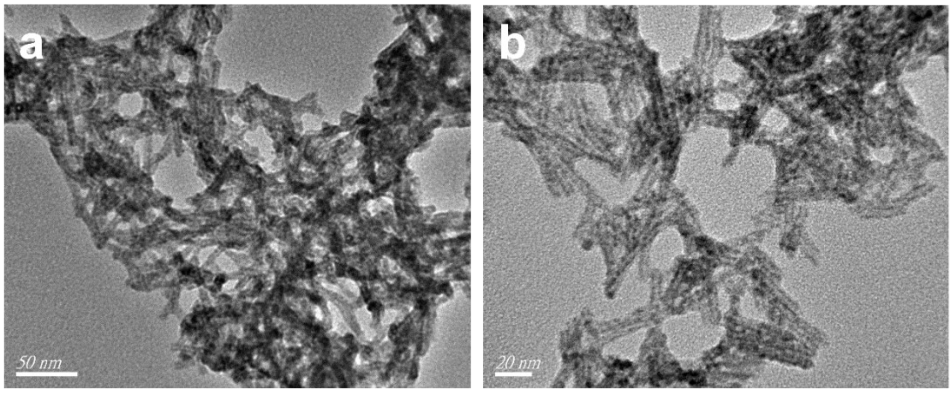

Figure S3. TEM images of prepared BOB nanotube materials.

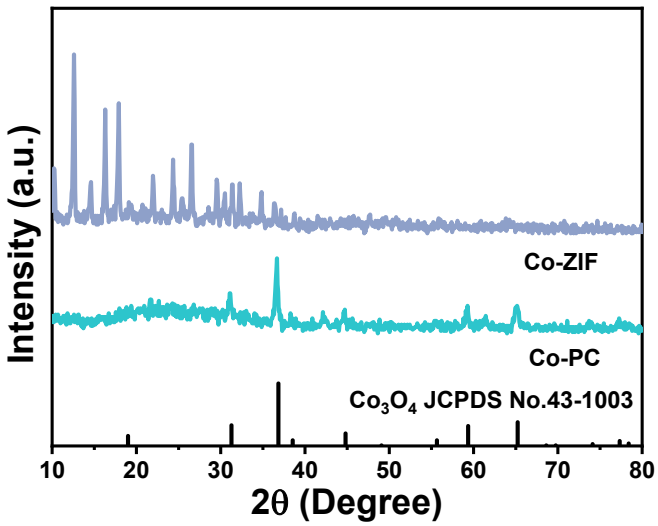

Figure S4. XRD patterns of the Co-ZIF template material and the corresponding obtained Co-PC material.

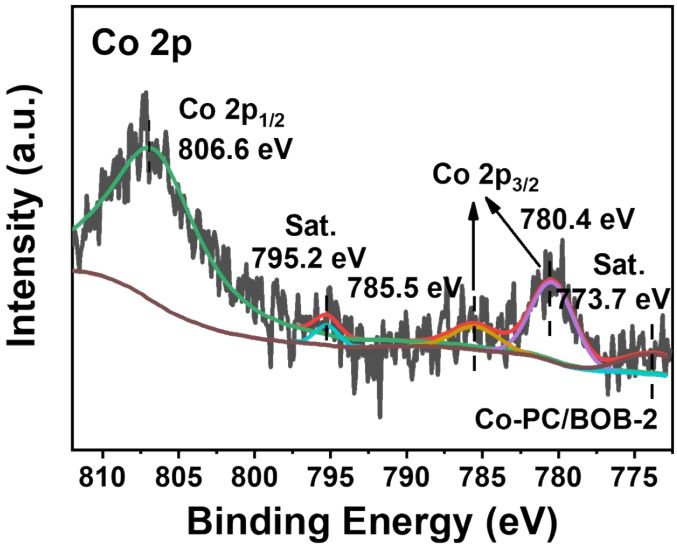

Figure S5. Co 2p high-resolution XPS spectrum of the Co-PC/BOB-2 composite.

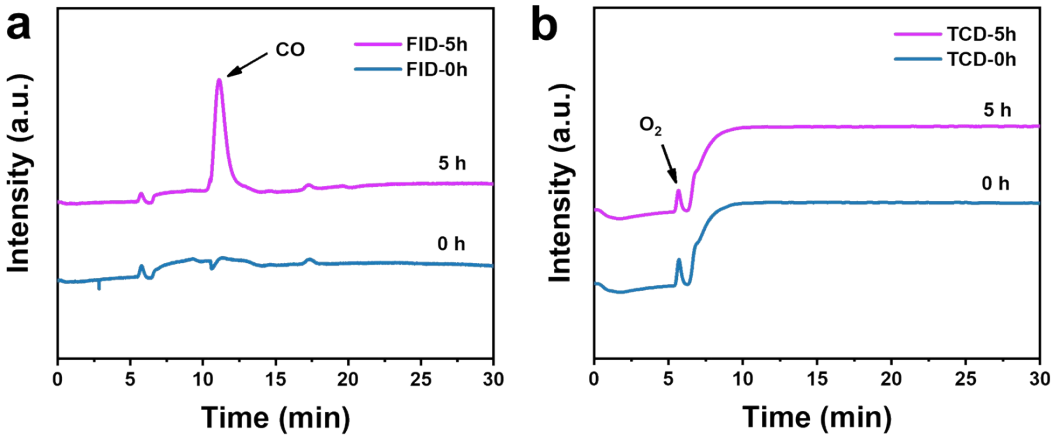

Figure S6. Original gas chromatography data of generated gaseous products over Co-PC/BOB-2 composite detected by (a) flame ionization detector (FID) and (b) thermal conductivity detector (TCD) (reaction for 5 h).

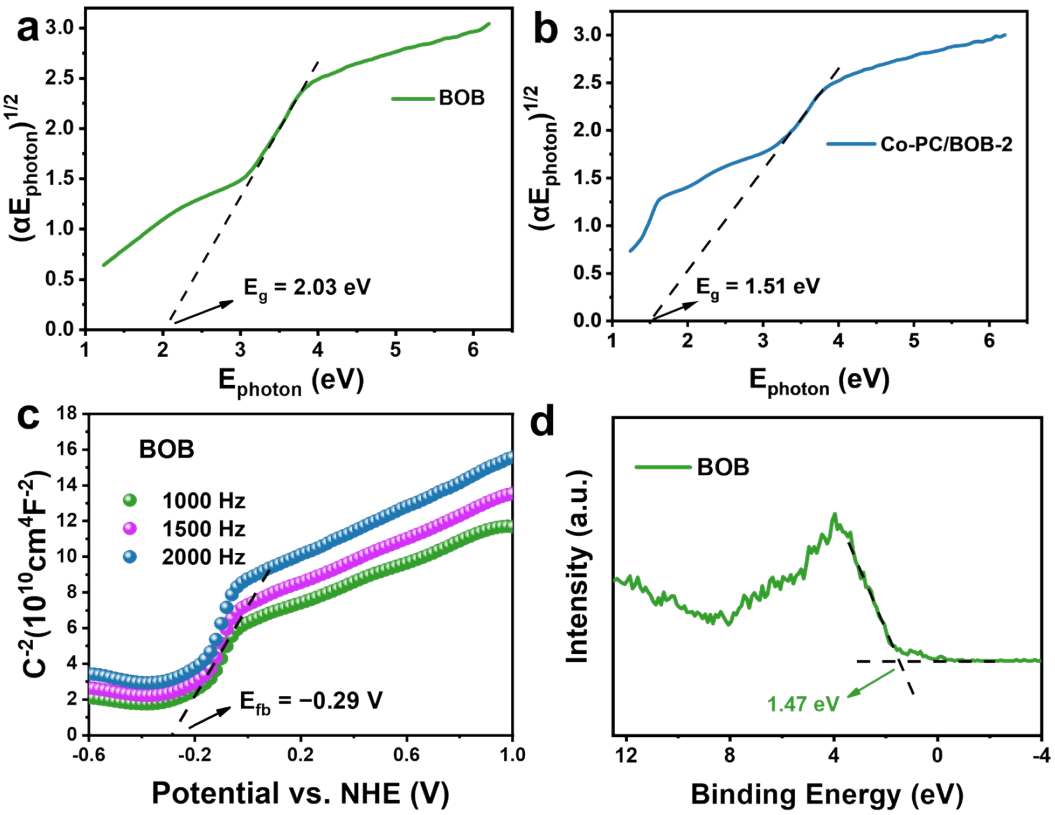

Figure S7. $(\alpha E_{photon})^{1/2}$ vs E_{photon} curve of (a) BOB nanotubes and (b) Co-PC/BOB-2. (c) Mott-Schottky plots of BOB obtained in 0.2 mol/L Na_2SO_4 solution (pH = 7). (d) XPS valence band spectra of the BOB.

The Co-PC shows a broad spectral range from ultraviolet to visible and near-infrared light absorption, significantly expanding the utilization range of light energy and overcoming the spectral limitations of pristine BOB nanotubes.[1] Therefore, compared to BOB monomer, the Co-PC/BOB composite exhibits a narrower bandgap and enhanced light absorption capacity.

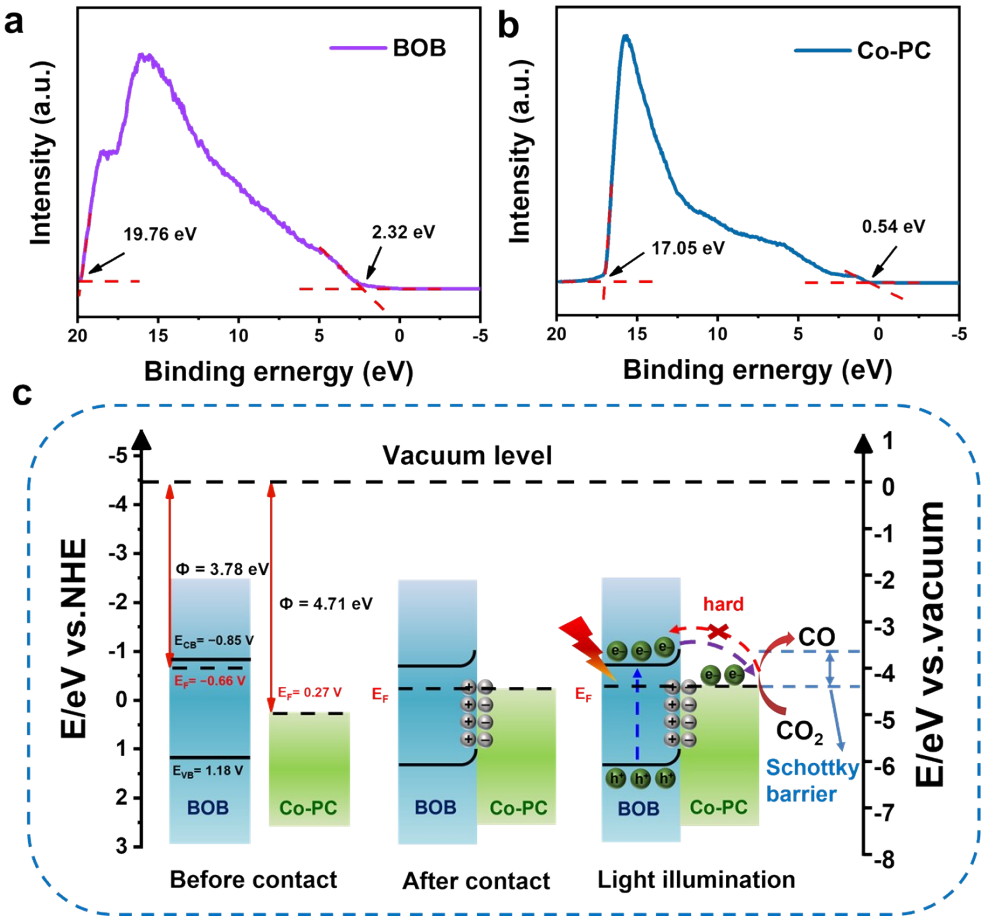

Figure S8. Figure S8. UPS spectra of (a) BOB and (b) Co-PC/BOB-2. (c) Energy band alignment of Co-PC/BOB-2 before contact, after contact, and light irradiation.

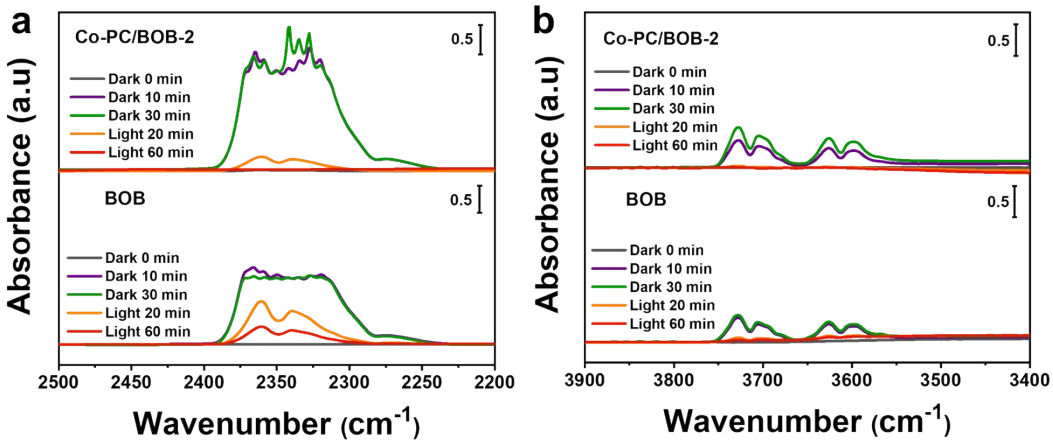

Figure S9. In-situ DRIFTS spectra for CO_2 interaction with BOB and Co-PC/BOB-2 in the dark.

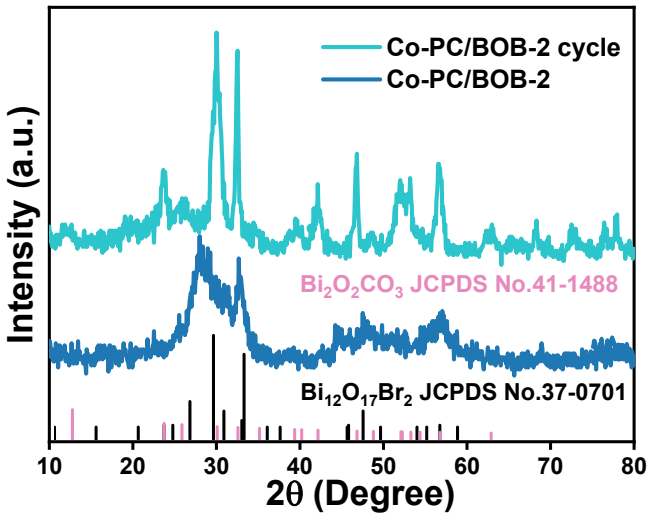

Figure S10. XRD patterns of Co-PC/BOB-2 before and after CO_2 photoreduction reaction.

$Bi_{12}O_{17}Br_2$ is a bismuth-rich halide bismuth oxide featuring a Sillén-type structure with alternating $[Bi_2O_2]^{2+}$ and Br^- layers, interconnected by interlayer van der Waals forces. The higher Bi/Br ratio in $Bi_{12}O_{17}Br_2$ implies fewer Br layers. Prolonged exposure to light can easily disrupt the interlayer van der Waals forces, accelerating the loss of Br^- and exposing the bismuth oxide layers,[2-3] which then react with CO_2 in the atmosphere or solution to form bismuth oxycarbonate.[4]

Table S2. Comparison of the CO_2 photoreduction to CO with other Bi-based catalysts.

Photocatalysts	Light sources	Reaction conditions	CO yield (μmol g^{-1} h^{-1})	Ref.
Co-PC/BOB-2	300 W Xe lamp	Liquid-solid, water	66.91	**This work**
BiOCl ultrathin nanosheets	300 W Xe lamp	Gas-solid, water	14.25	[5]
N-CQDs/Bi_4MoO_9-2	300 W Xe lamp	Liquid-solid, water	3.24	[6]
20-ZnO/BiOBr	300 W Xe lamp	Gas-solid, water	21.13	[7]
OV-rich $Bi_4O_5Br_2$ nanotubes	300 W Xe lamp	Gas-solid, water	19.56	[8]
BiOBr (001)	300 W Xe lamp	Gas-solid, water	4.45	[9]
s-BiOBr-mof1	300 W Xe lamp	Gas-solid, water	21.96	[10]
$Bi_{12}O_{17}Br_2$ nanotubes	300 W Xe lamp	Liquid-solid, water	34.5	[11]
Hollow $Bi_4O_5Br_2$	300 W Xe lamp	Gas-solid, water	3.16	[12]
BP-$Bi_{24}O_{31}Br_{10}$-0.5	300 W Xe lamp	Liquid-solid, water	39.80	[13]
$BiOIO_3$ single crystals	300 W Xe lamp	Gas-solid, water	17.33	[14]
Defective Bi_2MoO_6	300 W Xe lamp	Liquid-solid, water	3.62	[15]
OV-rich Bi_5O_7Br NWs	300 W Xe lamp with an AM 1.5 G filter	Gas-solid, water	18.04	[16]

References

[1] Yang, S.; Byun, W. J.; Zhao, F.; Chen, D.; Mao, J.; Zhang, W.; Peng, J.; Liu, C.; Pan, Y.; Hu, J.; et al. CO_2 Enrichment Boosts Highly Selective Infrared-Light-Driven CO_2 Conversion to CH_4 by UiO-66/Co_9S_8 Photocatalyst. Advanced Materials 2024, 36 (16), 2312616.

[2] Yu, H.; Huang, H.; Xu, K.; Hao, W.; Guo, Y.; Wang, S.; Shen, X.; Pan, S.; Zhang, Y. Liquid-Phase Exfoliation into Monolayered BiOBr Nanosheets for Photocatalytic Oxidation and Reduction. ACS Sustainable Chemistry & Engineering 2017, 5 (11), 10499-10508.

[3] Ye, L.; Deng, Y.; Wang, L.; Xie, H.; Su, F. Bismuth-Based Photocatalysts for Solar Photocatalytic Carbon Dioxide Conversion. ChemSusChem 2019, 12 (16), 3671-3701.

[4] Ma, J.; Yan, J.; Xu, J.; Ni, J.; Zhang, H.; Lu, L. Dynamic ion exchange engineering BiOI-derived $Bi_2O_2CO_3$ to promote CO_2 electroreduction for efficient formate production. Chemical Engineering Journal 2023, 455, 140926.

[5] Ding, C.; Ma, Z.; Han, C.; Liu, X.; Jia, Z.; Xie, H.; Bao, K.; Ye, L. Large-scale preparation of BiOX (X = Cl, Br) ultrathin nanosheets for efficient photocatalytic CO_2 conversion. Journal of the Taiwan Institute of Chemical Engineers 2017, 78, 395-400.

[6] Liu, Z.; Ji, M.; Zhao, J.; Zhang, Y.; Sun, X.; Shao, Y.; Li, H.; Yin, S.; Xia, J. Dual modulation steering electron reducibility and transfer of bismuth molybdate nanoparticle to boost carbon dioxide photoreduction to carbon monoxide. Journal of Colloid and Interface Science 2022, 610, 518-526.

[7] Shen, M.; Zhu, X.; Lin, L.; Li, H.; Wang, Y.; Liang, Q.; Zhou, M.; Li, Z.; Xu, S. MOFs-derived S-scheme ZnO/BiOBr heterojunction with rich oxygen vacancy for boosting photocatalytic CO_2 reduction. Separation and Purification Technology 2025, 353, 128620.

[8] Mao, D.; Hu, Y.; Yang, S.; Liang, J.; He, H.; Yang, S.; Xu, Z.; Sun, C.; Zheng,

S.; Jiang, Z.; et al. Oxygen-vacancy-induced charge localization and atomic site activation in ultrathin $Bi_4O_5Br_2$ nanotubes for boosted CO2 photoreduction. Chemical Engineering Journal 2023, 452, 139304.

[9] Wu, D.; Ye, L.; Yip, H. Y.; Wong, P. K. Organic-free synthesis of {001} facet dominated BiOBr nanosheets for selective photoreduction of CO_2 to CO. Catalysis Science & Technology 2017, 7 (1), 265-271.

[10] Yue, X.; Cheng, L.; Li, F.; Fan, J.; Xiang, Q. Highly Strained Bi-MOF on Bismuth Oxyhalide Support with Tailored Intermediate Adsorption/Desorption Capability for Robust CO_2 Photoreduction. Angewandte Chemie International Edition 2022, 61 (40), e202208414.

[11] Di, J.; Song, P.; Zhu, C.; Chen, C.; Xiong, J.; Duan, M.; Long, R.; Zhou, W.; Xu, M.; Kang, L.; et al. Strain-Engineering of $Bi_{12}O_{17}Br_2$ Nanotubes for Boosting Photocatalytic CO_2 Reduction. ACS Materials Letters 2020, 2 (8), 1025-1032.

[12] Jin, X.; Lv, C.; Zhou, X.; Xie, H.; Sun, S.; Liu, Y.; Meng, Q.; Chen, G. A bismuth rich hollow $Bi_4O_5Br_2$ photocatalyst enables dramatic CO_2 reduction activity. Nano Energy 2019, 64, 103955.

[13] Di, J.; Zhu, X.; Hao, G.; Zhu, C.; Chen, H.; Liu, Q.; Duan, R.; Hu, H.; Zhang, Y.; Xiong, J.; et al. Vacancy Pair-Induced Charge Rebalancing with Surface and Interfacial Dual Polarization for CO_2 Photoreduction. ACS Catalysis 2022, 12 (24), 15728-15736.

[14] Chen, F.; Ma, Z.; Ye, L.; Ma, T.; Zhang, T.; Zhang, Y.; Huang, H. Macroscopic Spontaneous Polarization and Surface Oxygen Vacancies Collaboratively Boosting CO_2 Photoreduction on $BiOIO_3$ Single Crystals. Advanced Materials 2020, 32 (11), 1908350.

[15] Di, J.; Zhao, X.; Lian, C.; Ji, M.; Xia, J.; Xiong, J.; Zhou, W.; Cao, X.; She, Y.; Liu, H.; et al. Atomically-thin Bi_2MoO_6 nanosheets with vacancy pairs for improved photocatalytic CO_2 reduction. Nano Energy 2019, 61, 54-59.

[16] Mao, D.; Yang, S.; Hu, Y.; He, H.; Yang, S.; Zheng, S.; Sun, C.; Jiang, Z.; Qu, X.; Wong, P. K. Efficient CO_2 photoreduction triggered by oxygen

vacancies in ultrafine Bi_5O_7Br nanowires. Applied Catalysis B: Environmental 2023, 321, 122031.